

# TCIP: Threshold-Controlled Iterative Pyramid Network for Deformable Medical Image Registration

Heming Wu<sup>1</sup>, Di Wang<sup>2</sup>, Tai Ma<sup>3</sup>, Peng Zhao<sup>4</sup>, Yubin Xiao<sup>4</sup>, Zhongke Wu<sup>5</sup>, Xing-Ce Wang<sup>5</sup>,  
Chuang Li<sup>6</sup>, Xuan Wu<sup>4,\*</sup>, You Zhou<sup>1,4,\*</sup>

<sup>1</sup>College of Software, Jilin University

<sup>2</sup>Joint NTU-UBC Research Centre of Excellence in Active Living for the Elderly, Nanyang Technological University

<sup>3</sup>College of Computer Science and Technology, Zhejiang University

<sup>4</sup>Key Laboratory of Symbolic Computation and Knowledge Engineering of Ministry of Education,

College of Computer Science and Technology, Jilin University

<sup>5</sup>School of Artificial Intelligence, Beijing Normal University

<sup>6</sup>First Hospital of Qinhuangdao

## Abstract

Although pyramid networks have demonstrated superior performance in deformable medical image registration, their decoder architectures are inherently prone to propagating and accumulating anatomical structure misalignments. Moreover, most existing models do not adaptively determine the number of iterations for optimization under varying deformation requirements across images, resulting in either premature termination or excessive iterations that degrades registration accuracy. To effectively mitigate the accumulation of anatomical misalignments, we propose the Feature-Enhanced Residual Module (FERM) as the core component of each decoding layer in the pyramid network. FERM comprises three sequential blocks that extract anatomical semantic features, learn to suppress irrelevant features, and estimate the final deformation field, respectively. To adaptively determine the number of iterations for varying images, we propose the dual-stage Threshold-Controlled Iterative (TCI) strategy. In the first stage, TCI assesses registration stability and with asserted stability, it continues with the second stage to evaluate convergence. We coin the model that integrates FERM and TCI as Threshold-Controlled Iterative Pyramid (TCIP). Extensive experiments on three public brain MRI datasets and one abdomen CT dataset demonstrate that TCIP outperforms the state-of-the-art (SOTA) registration networks in terms of accuracy, while maintaining comparable inference speed and a compact model parameter size. Finally, we assess the generalizability of FERM and TCI by integrating them with existing registration networks and further conduct ablation studies to validate the effectiveness of these two proposed methods.

## 1 Introduction

Deformable image registration aims to align the corresponding anatomical structures between a fixed and moving image pair by estimating a dense non-linear deformation field, with widespread real-world applications in medical image analysis (Cai et al. 2020; Rana, Hampson, and Dobie 2019). To estimate the deformation field, conventional methods perform separate optimizations for each image pair, incurring high computational costs (Fischer and Modersitzki 2008).

To improve efficiency, prior studies have leveraged Deep Learning (DL) methods for deformable image registration (Jia et al. 2022, 2023), with pioneering studies (Balakrishnan et al. 2018, 2019) primarily employing the U-Net networks to estimate the deformation field and warp the moving image. However, U-Net networks typically produce a single deformation field at the output layer, limiting their ability to accurately capture deformations that are large in both magnitude and complexity (Lv et al. 2022). To better address this challenge, certain studies adopted a cascaded registration scheme involving multiple subnetworks, each operating at a specific resolution (i.e., scale) to extract features and estimate a corresponding deformation field (De Vos et al. 2019; Mok and Chung 2020). This approach, while effective in handling large deformations, often redundantly re-extracts features at each subnetwork and fails to leverage previously encoded features (Wang, Ni, and Wang 2024).

To minimize unnecessary feature extraction, recent studies have proposed pyramid models (Kang et al. 2022; Liu et al. 2022; Ma et al. 2024; Meng et al. 2024) that employ a single encoder to extract multi-scale feature maps. Subsequently, at each scale, the decoding layer fuses the feature maps extracted from both the fixed and moving image branches to estimate the deformation field. The estimated deformation field is then passed to the subsequent decoding layer (see Figure 1(a)), thereby achieving coarse-to-fine estimation. Although pyramid architectures facilitate multi-scale feature extraction, their decoders may exacerbate the propagation and accumulation of anatomical structure misalignments, especially those stemmed from irrelevant information in deep, coarse-scale features. This exacerbation ultimately constrains the overall registration performance (Zhou et al. 2023). In addition, existing pyramid models often adopt vanilla residual decoders, which often lead to unnecessary computation resource utilization. Moreover, in scenarios involving large deformations, a one-pass estimation per scale typically fails to yield an accurate deformation field, necessitating iterative estimations at each scale. Consequently, SOTA models perform multiple estimations at each scale to iteratively optimize the deformation fields. For example, Wang, Ni, and Wang (2024) adopted a fixed

\*Corresponding Authors.

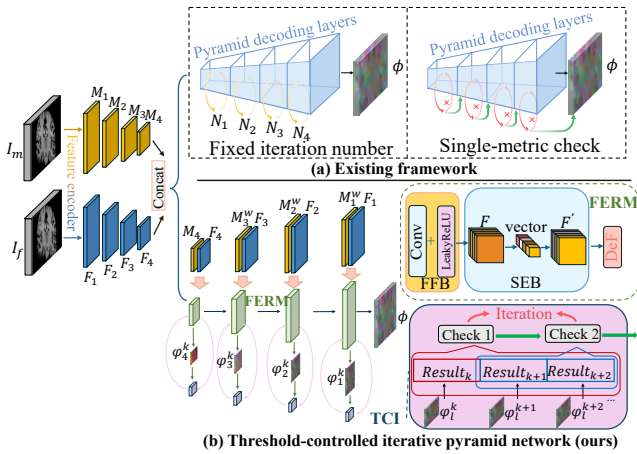


Figure 1: Illustration of the differences in decoding processes between existing pyramid models and our proposed TCIP. Sub-figure (a) portrays the existing models (Wang, Ni, and Wang 2024) and (Ma et al. 2024), which neither effectively prevent propagation and accumulation of anatomical structure misalignments nor adaptively determine the number of iterations. Sub-figure (b) depicts the proposed TCIP. At each decoding layer, TCIP employs our designed FERM to learn to suppress irrelevant features, thereby reducing misalignment accumulation. Subsequently, TCIP employs our novel dual-stage TCI strategy to adaptively determine the number of iterations for guiding FERM in the progressive optimization process of the deformation field.

number of iterations, while Ma et al. (2024) introduced a single-stage mechanism to dynamically determine the number of iterations at each scale. However, due to the diversity among image pairs, neither a fixed number of iterations nor a single-stage criterion may effectively adapt to varying deformation requirements, often resulting in premature termination or excessive iterations that degrades registration performance (see Tables 1 and 2).

To mitigate misalignment propagation and accumulation in pyramid architectures, we propose the Feature-Enhanced Residual Module (**FERM**) as the core component of the decoding layer, which can emphasize informative features. Specifically, FERM comprises three sequential blocks (see Figure 1(b)), namely Feature Fusion Block (FFB), Squeeze Excitation Block (SEB), and Deformation Field Estimator (DeF). Initially, at the  $l$ th scale, the residual FFB extracts anatomical semantic features from both the fixed and moving images, while preserving detailed original information. Subsequently, SEB applies channel-wise attention to reweight these extracted features (see Section 3.2), learning to suppress irrelevant ones. Finally, DeF estimates the deformation fields. By adopting this design, FERM achieves high-level registration performance with fewer parameters comparing to a vanilla residual decoder. Moreover, to adaptively determine the number of iterations for diverse image pairs, we propose the dual-stage Threshold-Controlled Iterative (**TCl**) strategy, which employs a sliding window to dynamically track the estimated deformation fields and quan-

tifies each by the similarity difference between the warped image  $I_m^w$  and the fixed image  $I_f$ . TCI then assesses the stability of deformation (i.e., first stage) by computing the standard deviation of all similarity differences within this window. Upon reaching stability (see Section 3.3), TCI further evaluates convergence (i.e., second stage) by measuring the change between similarity differences of the two most recently estimated deformation fields within this window. TCI is designed to be efficient to enable adaptive determination of the number of iterations for each scale of the underlying image pair, without significantly increasing registration time (see Section 4.1). We coin the network that integrates FERM and TCI as the Threshold-Controlled Iterative Pyramid (**TCIP**) network.

The key contributions of this work are as follows:

i) We propose the lightweight FERM as the core component of the decoding layer, which integrates residual blocks and channel-wise attention to extract anatomical features and learn to suppress irrelevant information, thereby mitigating misalignment accumulation.

ii) We propose the dual-stage TCI strategy, which monitors the stability and convergence of recent registration results to adaptively determine the number of iterations for image pairs with varying deformation requirements.

iii) To assess the performance of TCIP, we conduct extensive experiments on three public brain Magnetic Resonance Imaging (MRI) datasets and one abdomen Computed Tomography (CT) dataset. The results demonstrate that TCIP outperforms SOTA registration models in accuracy across all datasets, while achieving on-par inference speed and a compact model size. Moreover, generalization and ablation studies further validate the effectiveness of FERM and TCI.

## 2 Related Work

**Deep Learning (DL) Registration Models:** DL models have become the mainstream for registration tasks due to their advantages in inference speed and accuracy compared to conventional registration methods (Balakrishnan et al. 2019). Pioneer DL models primarily employed U-Net architectures, which estimate only a single deformation field at the final output layer and consequently struggle to accommodate complex deformations (Wang and Wang 2025). To better overcome this limitation, certain studies (De Vos et al. 2019; Zhao et al. 2019a,b) proposed cascaded registration networks, which employ multiple sub-networks to extract features at distinct resolutions and estimate the corresponding deformation fields. Although these models achieve moderate accuracy improvements, they perform repeated encoding and decoding, leading to redundant feature extraction and elevated computing overhead (Ma et al. 2024).

To minimize redundant feature processing, recent studies (Liu et al. 2022) proposed the pyramid network, which adopts a single encoder followed by multiple decoding layers to estimate hierarchical deformation fields for continuous coarse-to-fine warping images. Although this architecture facilitates effective multi-scale feature extraction and progressive deformation estimation, it may exacerbate the propagation and accumulation of anatomical structure misalignments, especially those stemmed from irrelevant infor-

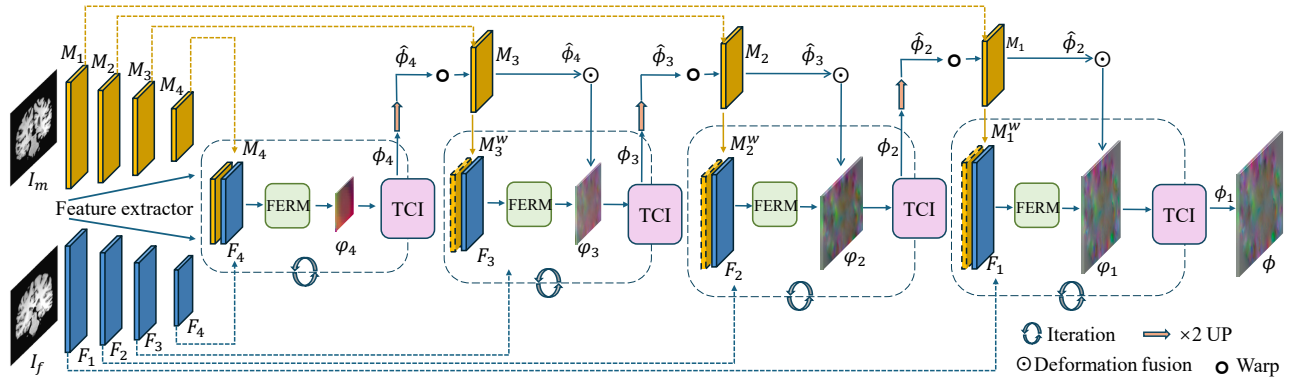


Figure 2: Overall TCIP model architecture. A weight-sharing encoder first extracts multi-scale feature maps  $\{F_l\}$  and  $\{M_l\}$  for the fixed image  $I_f$  and the moving image  $I_m$ , respectively. In the subsequent decoding layers, TCIP employs FERM to emphasize informative features and estimate deformation field  $\phi_l$ , while TCI adaptively determines the number of iterations for each decoding layer, enabling progressive optimization of  $\phi_l$ . Notably, the encoder processes higher-resolution feature maps first, while the decoder begins deformation estimation on the lowest-resolution maps and proceeds to finer scales.

mation in deep, coarse-scale features which ultimately affect the overall registration performance (Zhou et al. 2023). To better overcome this limitation, we propose FERM, which learns to suppress irrelevant features through feature weighting in the decoding layers, thereby mitigating misalignment propagation. Moreover, FERM excels at capturing anatomical details, ensuring the accuracy and consistency of deformation fields at each scale (see Section 3.2).

**Iterative Strategy in Pyramid Models:** For small deformations, prior pyramid models (Kang et al. 2022) estimated only a single deformation field per decoding layer (each corresponding to one scale). Consequently, each scale requires iterative estimations to refine the deformation field. For example, Wang, Ni, and Wang (2024) proposed RDP, which performs a predefined number of iterations for each scale to refine the deformation field. Inevitably, this fixed number of iterations lacks adaptability to varying deformation requirements. To adaptively determine the number of iterations, Ma et al. (2024) proposed a single-stage mechanism, which evaluates convergence by monitoring differences between two successive registration results. However, relying on a single-metric check only captures partial information and may lead to premature iteration termination, potentially compromising the overall registration accuracy. To dynamically determine when to stop iterative optimization, we propose a dual-stage mechanism, which evaluates the stability of historical registration results and convergence subsequently (see Section 3.3).

### 3 Threshold-Controlled Iterative Pyramid

The architecture of **TCIP** is schematically illustrated in Figure 2. In this section, we first introduce **FERM**, which excels at extracting anatomical structure details and learn to suppress irrelevant features to mitigate misalignment. We then introduce the dual-stage **TCI** strategy, which adaptively determines the number of iterations for optimization.

#### 3.1 Overview of TCIP

The proposed TCIP comprises a multi-scale encoder and a multi-layer decoder. TCIP first employs a weight-sharing feature encoder to extract multi-scale feature map sets  $\{F_l\}$  and  $\{M_l\}$ , where  $l \in \{1, \dots, 4\}$  (following prior arts in this field: (Kang et al. 2022; Ma et al. 2024)), from the fixed image  $I_f$  and moving image  $I_m$ , respectively. Specifically, TCIP adopts the encoder used in (Ma et al. 2024), which comprises four convolutional blocks, each comprising a 3D convolutional layer with a LeakyReLU activation function, followed by average pooling that halves the spatial dimensions of the feature maps. Then, for the  $l$ th scale (i.e., the  $l$ th decoding layer), TCIP applies FERM to process  $\{F_l\}$  and  $\{M_l\}$ , extracting anatomical structure details and learning to suppress irrelevant features, to estimate the corresponding deformation fields (see Section 3.2). To adaptively determine the number of iterations in each decoding layer, TCIP relies on TCI, which monitors the similarity difference of the recently estimated registration results within a sliding window (see Section 3.3).

#### 3.2 Feature-Enhanced Residual Module (FERM)

To effectively capture anatomical structure details while learning to suppress irrelevant features, we propose the Feature-Enhanced Residual Module (FERM) as the core component of the decoder for estimating deformation fields. As shown in Figure 3, FERM comprises three blocks, namely Feature Fusion Block (FFB), Squeeze Excitation Block (SEB), and Deformation Field Estimator (DeF). Specifically, for the fourth decoding layer (leftmost decoding layer in Figure 2), FFB directly fuses  $F_4$  and  $M_4$ , and then extracts the fused features  $R_4$ . For layers  $l \in \{1, 2, 3\}$ , FFB first upsamples the deformation field  $\phi_{l+1}$  by a factor of 2 using linear interpolation to obtain  $\hat{\phi}_{l+1}$  at the scale of  $M_l$ , and then warps  $M_l$  to obtain  $M_l^w$ . Then, FFB fuses  $F_l$  and  $M_l^w$  and extracts the features  $R_l \in \mathbb{R}^{C \times H \times W \times D}$ , where  $C, H, W, D$  denote the number of channels, height,

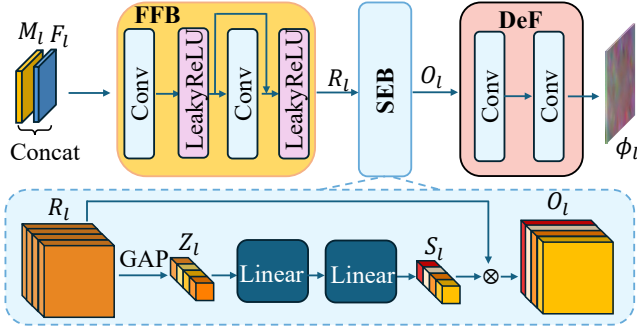


Figure 3: Depiction of the proposed FERM, comprising the FFB, SEB, and DeF modules. FFB is responsible for extracting anatomical structure details. SEB suppresses irrelevant features to mitigate anatomical structure misalignment accumulation. DeF estimates the deformation fields.

width, and depth of the image, respectively. Formally,

$$R_l = \begin{cases} \text{FFB}(|M_4, F_4|), & l = 4, \\ \text{FFB}(|M_l^w, F_l|), & l \in \{1, 2, 3\}, \end{cases} \quad (1)$$

where  $|\cdot|$  denotes the concatenation operator. FFB comprises two 3D convolutional layers  $\mathcal{C}1$  and  $\mathcal{C}2$ , each followed by a LeakyReLU activation function  $\gamma$ . In the first convolutional layer  $\mathcal{C}1$ , FFB reduces the concatenated channel dimension from  $2C$  to  $C$ . A residual connection adds the output of the first activation to the second convolutional layer output, preserving original image features while enabling the extraction of high-level anatomical structure details. The FFB function is formally defined as follows:

$$\text{FFB}(\cdot) = \gamma(\mathcal{C}2_{C \rightarrow C}(\gamma(\mathcal{C}1_{2C \rightarrow C}(\cdot))) + \gamma(\mathcal{C}1_{2C \rightarrow C}(\cdot))). \quad (2)$$

Subsequently, FERM extends the 2D SEB (Hu, Shen, and Sun 2018) to a 3D variant to suppress irrelevant features in  $R_l$ , thereby mitigating propagation and accumulation of anatomical misalignment. Specifically, SEB first employs global average pooling to compress spatial dimensions and extract global informative features, producing the channel descriptor vector  $Z_l \in \mathbb{R}^C$  as follows:

$$Z_{l,c} = \frac{1}{H \cdot W \cdot D} \sum_{i=1}^H \sum_{j=1}^W \sum_{d=1}^D R_{l,c,i,j,d}, \quad (3)$$

where  $c \in \{1, \dots, C\}$ . Then, SEB applies two fully connected layers with LeakyReLU  $\gamma$  and sigmoid  $\sigma$  activation functions to compute the channel weight vector  $S_l$  as follows:

$$S_l = \sigma(W_2 \gamma(W_1 Z_l)), \quad (4)$$

where  $W_1 \in \mathbb{R}^{\frac{C}{r} \times C}$  and  $W_2 \in \mathbb{R}^{C \times \frac{C}{r}}$ . The hyperparameter  $r$  denotes the reduction ratio, which is used to gauge the computational cost. The first linear layer reduces the dimensionality of  $Z_l$  to  $\frac{C}{r}$ , for efficient channel-wise compression and information aggregation. The second linear layer then restores the dimensionality back to  $C$ . By adopting this design, SEB extracts the global contextual information from each channel through a compression process. SEB

then models inter-channel dependencies and recalibrates the channels via an expansion process, thereby capturing global dependencies between channels. Subsequently, the resulting weight vector  $S_l$  is applied to  $R_l$  via per-channel element-wise multiplication  $*$ , yielding the enhanced feature map  $O_l \in \mathbb{R}^{C \times H \times W \times D}$ , defined as follows:

$$O_{l,c} = R_{l,c} * S_{l,c}, c \in \{1, \dots, C\}, \quad (5)$$

By differentiating channels with associated weights (i.e.,  $S_l$ ), SEB emphasizes deformation-relevant features while suppressing irrelevant information (see Table 5).

Finally, DeF processes  $O_l$  via two convolutional layers  $\mathcal{C}3$  and  $\mathcal{C}4$  to estimate the deformation field  $\phi_l$  as follows:

$$\phi_l = \mathcal{C}4_{\frac{C}{2} \rightarrow 3}(\mathcal{C}3_{C \rightarrow \frac{C}{2}}(O_l)). \quad (6)$$

Layer  $\mathcal{C}3$  halves the channel dimension from  $C$  to  $\frac{C}{2}$ , while  $\mathcal{C}4$  outputs three channels corresponding to the 3D deformation field. Notably, unlike the decoder adopted by IIRP (Ma et al. 2024), which relies solely on multiple sequential residual blocks to estimate the deformation field, FERM integrates lightweight channel attention alongside a minimal number of residual blocks, designed to yield elevated performance with fewer parameters (see Table 1).

### 3.3 Threshold-Controlled Iterative (TCI)

The number of iterations is crucial for optimizing the deformation field; early termination may yield suboptimal accuracy, while excessive iterations can introduce misalignment and consume unnecessary computing resources. To adaptively determine the number of iterations for varying image pairs, we propose a dual-stage TCI strategy to evaluate both stability and convergence using historical registration results to dynamically determine when to stop. As shown in Figure 4, at the  $l$ th decoding layer, TCI employs a sliding window  $W_l$  to dynamically track the similarity differences of  $t$  number of recently estimated registration results. To compute the similarity difference  $s_l^k$  between the warped image  $I_m^w$  and the fixed image  $I_f$  at the  $k$ th iteration, TCI first up-samples the deformation field  $\varphi_l^k$  estimated by DeF, yielding the upsampled deformation field  $\hat{\varphi}_l^k$  at the original moving image resolution. The upsampling is implemented via linear interpolation with a factor of  $2^{l-1}$ . Next, the upsampled deformation field  $\hat{\varphi}_l^k$  provides a displacement vector for each voxel and is applied to the moving image  $I_m$  to produce the corresponding warped image  $I_m^w$ , i.e.,  $I_m^w = I_m \circ \hat{\varphi}_l^k$ , where  $\circ$  denotes the deformation operation, implemented via the Spatial Transformer Network (Jaderberg et al. 2015). Finally,  $s_l^k$  is computed as follows:

$$s_l^k = \text{sim}(I_f, I_m^w), \quad (7)$$

where  $\text{sim}(\cdot)$  denotes the similarity metric. In this work, we always adopt Normalized Cross-Correlation (NCC) to compute the registration similarity after examining various candidates (see Appendix F).

After obtaining the similarity differences of  $t$  number of recently estimated registration results, TCI evaluates their stability and convergence in a dual-stage process, respectively. In the first stage, TCI assesses stability by computing

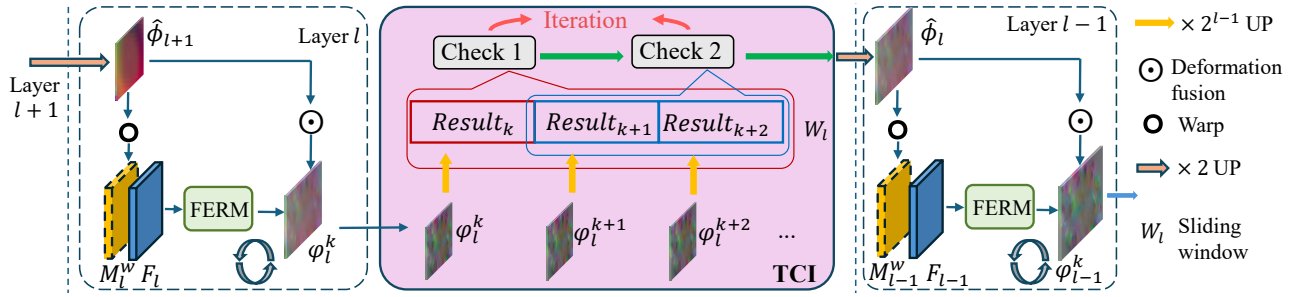


Figure 4: Depiction of the proposed TCI strategy, which determines when to stop the iteration through a dual-stage mechanism. TCI first checks whether the std  $\varepsilon_l$  of similarity differences across all historical registration results in  $W_l$  is lower than a threshold  $\delta_s$ . If yes, TCI further computes the change  $\Delta s$  between similarity differences of the two most recent registration results in  $W_l$ . If  $\Delta s$  is smaller than another threshold  $\delta_c$ , it is considered that the appropriate stopping criteria have been reached.

---

Algorithm 1: Registration process in the  $l$ th decoding layer

---

- 1: **Input:**  $(l + 1)$ th deformation field  $\hat{\phi}_{l+1}$ , feature maps  $F_l, M_l$ , original images  $I_f, I_m, W_l, k \leftarrow 1$
  - 2: **Output:**  $l$ th deformation field  $\phi_l$
  - 3:  $\varphi_l^{k-1} \leftarrow \hat{\phi}_{l+1}$  #If  $l = 4$ , this step is skipped
  - 4: **while**  $k \leq k_{max}$  **do**
  - 5:  $M_l^w \leftarrow M_l \circ \varphi_l^{k-1}$  #If  $l = 4$ , this step is skipped
  - 6:  $\varphi_l^k \leftarrow \text{FERM}(M_l^w, F_l)$  #If  $l = 4$ , replace  $M_l^w$  with  $M_4$
  - 7:  $\varphi_l^k \leftarrow \varphi_l^{k-1} \circ \varphi_l^k + \varphi_l^k$  #If  $l = 4 \& k = 1$ , this step is skipped. If  $l \neq 4 \& k = 1$ , replace  $\varphi_l^{k-1}$  with  $\hat{\phi}_{l+1}$
  - 8:  $\hat{\varphi}_l^k \leftarrow \text{upsample}(\varphi_l^k, 2^{l-1})$
  - 9:  $s_l^k \leftarrow \text{sim}(I_f, I_m \circ \hat{\varphi}_l^k)$  #see (7)
  - 10: **if**  $\text{len}(W_l) \geq t$  **then** #TCI
  - 11:  $\varepsilon_l \leftarrow \text{std}(W_l)$  #see (8)
  - 12: **if**  $\varepsilon_l \leq \delta_s$  **then** #Stage 1: assess stability
  - 13:  $\Delta s \leftarrow s_l^k - s_l^{k-1}$  #see (9)
  - 14: **if**  $\Delta s \leq \delta_c$  **then** #Stage 2: assess convergence
  - 15: **return**  $\hat{\phi}_l \leftarrow \text{upsample}(\varphi_l^k, 2)$
  - 16: **append**  $s_l^k$  to  $W_l$  #If  $\text{len}(W_l) = t + 1$ , remove  $s_l^{k-t}$  from  $W_l$
  - 17:  $k \leftarrow k + 1$
  - 18: **end while**
- 

the standard deviation  $\varepsilon_l$  of similarity differences  $s_l^k$  within the window  $W_l = \{s_l^{k-t+1}, \dots, s_l^k\}$ , defined as follows:

$$\varepsilon_l = \text{std}(W_l). \quad (8)$$

If  $\varepsilon_l$  falls below the predefined stability threshold  $\delta_s$ , the most recent  $t$  number of deformation fields are deemed stable. TCI then proceeds to the subsequent convergence evaluation stage. Otherwise, an additional iteration is performed without the necessity to continue the following stage.

In the subsequent convergence evaluation stage, TCI further computes the change in similarity differences, denoted as  $\Delta s$ , between the two most recent iterations within  $W_l$ , which is defined as follows:

$$\Delta s = s_l^k - s_l^{k-1}. \quad (9)$$

If  $\Delta s$  falls below the predefined convergence threshold  $\delta_c$ , the deformation field at the  $k$ th iteration is deemed con-

verged, the iteration terminates, and the deformation field  $\phi_l$  is passed to the  $(l - 1)$ th layer as input (see Figure 2). Otherwise, additional iterations continue at the  $l$ th layer. Following (Ma et al. 2024), TIC also leverages a predefined maximum number of iterations  $k_{max}$  to avoid rare non-convergence situations. The pseudocode of TCI is presented in Algorithm 1.

Notably, our TCI fundamentally differs from IIRP’s single-stage method (Ma et al. 2024), which performs only one similarity check between two consecutive registrations. Such a single-stage check, constrained by the stochastic nature of convergence, may lead to premature termination. In contrast, TCI introduces a two-stage evaluation strategy. Owing to the additional stability check, TCI makes more informed iteration-stopping decisions while maintaining comparable inference time (see Table 4). In addition, because IIRP’s decoder comprises multiple residual blocks, applying a single-stage strategy during training is highly memory-intensive; consequently, IIRP activates this strategy during inference only. By contrast, TCIP’s lightweight FERM decoding layer enables the integration of TCI for both training and inference. This joint optimization of the network and iteration controller from the commencement of training enhances registration performance without prolonging the computation significantly (see Tables 1 and 2).

### 3.4 Loss Function

Being an unsupervised registration network, similar to the prior SOTA model (Ma et al. 2024), TCIP employs NCC to evaluate the loss between the fixed image  $I_f$  and the warped moving image  $I_m^w$ , which is defined as follows:

$$\mathcal{L}_{ncc}(I_f, I_m^w) = \frac{\sum_{p_i} (I_f(p_i) - \bar{I}_f(p)) (I_m^w(p_i) - \bar{I}_m^w(p))}{\sqrt{\sum_{p_i} (I_f(p_i) - \bar{I}_f(p))^2 \sum_{p_i} (I_m^w(p_i) - \bar{I}_m^w(p))^2}}, \quad (10)$$

where  $\Omega$  denotes the entire volume domain (i.e., the set of all voxels of the fixed image),  $p_i$  denotes the  $i$ th voxel within  $p$ ’s local neighborhood (i.e., the cubic patch of size  $n^3$  centered at  $p$ ),  $\bar{I}_f(p)$  and  $\bar{I}_m^w(p)$  denote the averaged voxel value of  $I_f(p)$  and  $I_m^w(p)$ , respectively, computed over the corre-

sponding neighborhoods.

Moreover, to enforce the smoothness of the deformation field, we incorporate the  $L_2$ -norm  $\|\cdot\|$  on the gradient of  $\phi$ :

$$\mathcal{L}_{smooth}(\phi) = \sum_{p \in \Omega} \|\nabla \phi(p)\|^2. \quad (11)$$

Therefore, the total loss in TCIP is defined as follows:

$$\mathcal{L}_{total}(I_f, I_m) = \mathcal{L}_{ncc}(I_f, I_m^w) + \lambda \mathcal{L}_{smooth}(\phi), \quad (12)$$

where  $\lambda$  denotes the hyperparameter used to leverage the loss function.

## 4 Experimental Results

To assess the performance of TCIP, we conduct extensive experiments on three public MRI datasets, namely LPBA (Shattuck et al. 2008), IXI (Avants et al. 2009), and Mindboggle (Klein and Tourville 2012), and one abdomen CT dataset FLARE (Ma et al. 2022). Detailed descriptions of these datasets, evaluation metrics, and experimental setups, are provided in Appendix A.

### 4.1 Comparison with Baseline Models

To benchmark the performance of TCIP, we choose two U-Net models, namely VM (Balakrishnan et al. 2019) and TM (Chen et al. 2022), two cascaded models, namely RCN (Zhao et al. 2019a) and SDH (Zhou et al. 2023), and six multi-scale pyramid models, namely RDN (Hu et al. 2022), PR++ (Kang et al. 2022), I2G (Liu et al. 2022), RDP (Wang, Ni, and Wang 2024), IIRP (Ma et al. 2024), and SACB (Cheng et al. 2025) as baseline models. Table 1 presents the performance of different registration models on the Mindboggle, LPBA, and IXI datasets, measured using the Dice (Dice 1945), Jacobian determinant ( $|J_\phi|_{<0}$ ), and inference time (s) metrics. Appendix B presents HD95 (Huttenlocher, Klanderman, and Rucklidge 1993), ASSD (Taha and Hanbury 2015), and MSE metrics for these registration models across all three datasets. Table 2 presents the performance of different registration models (competing pyramid models in Table 1) on the FLARE dataset. The experimental results shown in both tables demonstrate that TCIP outperforms all the other registration models on the Dice metric across all four datasets. Unlike SACB, which estimates the deformation field only once per decoding layer, TCIP employs TCI to adaptively determine the number of iterations at each layer, thereby yielding superior performance, achieving Dice improvements of 1.3%, 0.2%, 0.2%, and 0.5% on the four datasets, respectively. Notably, RDP and IIRP also employ iterative strategies. However, RDP adopts a fixed number of iterations and IIRP relies on a single-stage stopping criterion evaluation, both of which lead to inferior performance. In contrast, our TCIP employs TCI with a dual-stage strategy at each decoding layer, thereby achieving elevated performance while incurring only a marginal increase in inference time over IIRP. Furthermore, FERM is designed to be efficient to excel at extracting anatomical structure details and suppresses irrelevant features, thereby enabling TCIP to achieve superior performance with only approximately 80% of the parameters needed by IIRP.

Figure 5 visualizes the registration results on the Mindboggle and LPBA datasets. Performance differences among models are more noticeable in the three structural regions of the brain images, highlighted by red, yellow, and blue boxes. These visualizations further demonstrate that the moving images, after being warped by the deformation fields produced by TCIP, align more closely with fixed images. Additionally, we perform quantitative analyses of specific regions in the left and right hemispheres to further illustrate variations in anatomical structure registration performance across different models. The results, as presented in Appendix C, further demonstrate the advantages of TCIP.

### 4.2 Generalizability of FERM and TCI

To demonstrate the generalizability of FERM and TCI, we integrate each into existing registration models and report the results in Tables 3 and 4, respectively. Table 3 shows that replacing the decoder with FERM yields consistent performance gains across all three pyramid models, showcasing FERM’s superior ability to suppress irrelevant features. Furthermore, Table 4 demonstrates that substituting IIRP’s original iterative strategy with TCI yields performance improvement, underscoring the advantage of TCI in determining the number of iteration dynamically.

### 4.3 Ablation Studies

We further conduct ablation studies to assess the effectiveness of the two key FERM modules, namely FFB and SEB. The performance of variants w/o FFB and/or SEB are shown in Table 5. As shown, the variant with neither FFB and SEB yields the lowest performance, indicating that relying solely on DeF is insufficient to capture complex deformation patterns, leading to higher registration errors. Furthermore, removing either FFB or SEB degrades performance relative to the intact FERM, demonstrating that the integration of them both enhances the network’s ability to accurately capture fine structural details and suppress irrelevant features, thereby significantly improving registration accuracy.

In addition, we investigate the performance of four TCI configurations on the IXI dataset. Specifically, TCI-1 performs only convergence evaluation, TCI-2 performs only stability evaluation, TCI-3 evaluates convergence before stability, and TCI-4 evaluates stability before convergence (the configuration adopted in TCIP). Table 6 shows that TCI-4 performs best, showcasing the appropriateness of TCI design.

Finally, Appendices D~G assess the effectiveness of TCI across different decoding layers and the influence of varying values of thresholds  $\delta_1$  and  $\delta_2$ , the choice of similarity metric, and the window size  $t$ , respectively.

## 5 Conclusion

We propose the deformable image registration network TCIP, which employs FERM to extract anatomical structure details and learn to suppress irrelevant features. Additionally, we introduce the dual-stage TCI strategy to determine the number of iterations. The results on four datasets demonstrate the effectiveness of TCIP. Generalizability and ablation studies validate the effectiveness of FERM and TCI.

Table 1: Performance comparison of different registration models on the Mindboggle, LPBA, and IXI datasets

	Model	Mindboggle			LPBA			IXI			#Param
		Dice(%) $\uparrow$	Time(s)	$ J_\phi <0\downarrow$	Dice(%) $\uparrow$	Time(s)	$ J_\phi <0\downarrow$	Dice(%) $\uparrow$	Time(s)	$ J_\phi <0\downarrow$	
U-Net	VM (CVPR'18)	56.0	<b>0.09</b>	<0.7%	65.1	<b>0.02</b>	<0.3%	75.9	<b>0.01</b>	<0.2%	<b>319.4K</b>
	TM (MIA'22)	61.5	0.10	<1.0%	67.0	0.10	<0.78%	76.9	0.03	<0.43%	45650.3K
Cascaded	RCN (ICCV'19)	63.4	0.19	<0.8%	71.4	0.05	<0.007%	78.6	0.06	<0.01%	958.1K
	SDH (TMI'23)	63.6	0.82	<0.2%	70.5	0.77	<0.4%	79.3	0.08	<0.2%	17862.0K
Pyramid	RDN (JBHI'22)	62.5	0.08	<0.03%	70.6	0.04	<0.05%	78.8	0.02	<0.06%	28653.2K
	PR++ (MIA'22)	63.1	0.47	<0.5%	70.4	0.64	<0.07%	79.3	0.07	<0.06%	1208.0K
	I2G (MMMI'22)	62.5	0.51	<0.03%	71.7	0.06	<0.006%	79.3	0.51	<0.02%	865.2K
	RDP (TMI'24)	65.5	0.37	< <b>0.003%</b>	73.1	0.26	< <b>0.0002%</b>	80.4	0.11	< <b>0.003%</b>	8922.4K
	IIRP (CVPR'24)	65.8	0.12	<0.006%	72.2	0.10	<0.02%	80.4	0.09	<0.02%	410.1K
	SACB (CVPR'25)	65.1	2.08	<0.06%	73.1	1.45	<0.02%	80.3	1.02	<0.03%	1105.6K
	<b>TCIP (ours)</b>	<b>66.4</b>	0.16	<0.004%	<b>73.3</b>	0.13	<0.001%	<b>80.5</b>	0.09	<0.004%	330.4K

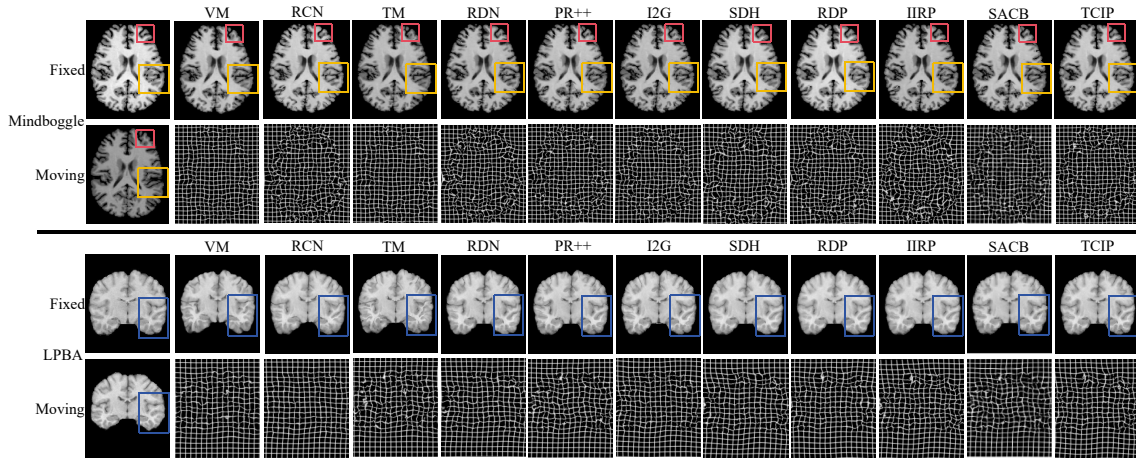


Figure 5: Visualization of registration results and corresponding deformation fields across different models.

Table 2: Performance comparison on the FLARE dataset

Model	Dice (%) $\uparrow$	Time (s)	$ J_\phi <0\downarrow$
PR++ (MIA'22)	60.2	0.07	<1.4%
RDP (TMI'24)	73.0	0.08	< <b>0.03%</b>
IIRP (CVPR'24)	73.8	<b>0.03</b>	<2.0%
SACB (CVPR'25)	74.3	0.13	<0.7%
<b>TCIP (ours)</b>	<b>74.8</b>	0.06	<0.2%

Table 3: The generalizability of FERM on the IXI dataset

Model	Dice (%)	MSE ( $10^{-3}$ )
I2G (+ FERM)	79.3 (79.7)	0.40 (0.39)
PR++ (+ FERM)	79.3 (79.4)	0.36 (0.37)
IIRP (+ FERM)	80.4 (81.2)	0.23 (0.19)

Table 4: The generalizability of TCI

	Mindboggle			LPBA		
	Dice (%)	MSE	Time (s)	Dice (%)	MSE	Time (s)
IIRP	65.9	4.16	<b>0.12</b>	72.2	0.62	<b>0.10</b>
IIRP + TCI	<b>66.2</b>	<b>3.56</b>	0.14	<b>73.0</b>	<b>0.61</b>	0.14

Table 5: Ablation study on different FERM modules

FFB	SEB	Mindboggle		LPBA		IXI	
		Dice(%)	MSE	Dice(s)	MSE	Dice(s)	MSE
$\times$	$\times$	65.3	4.16	72.4	0.79	80.1	0.26
$\times$	$\checkmark$	65.8	4.10	72.5	0.73	80.3	0.24
$\checkmark$	$\times$	65.9	4.02	72.7	0.71	80.4	0.24
$\checkmark$	$\checkmark$	<b>66.4</b>	<b>3.97</b>	<b>73.3</b>	<b>0.61</b>	<b>80.5</b>	<b>0.23</b>

Table 6: Ablation study on different TCI configurations

	TCI-1	TCI-2	TCI-3	TCI-4
Dice (%)	80.40	80.31	80.44	<b>80.58</b>
MSE ( $10^{-3}$ )	0.234	0.252	0.232	<b>0.230</b>

Currently, we extend the original 2D SEB into a 3D variant to suppress irrelevant features. Going forward, we believe further improvement is achievable by extending SEB to incorporate local importance pooling to emphasize key regions rather than relying solely on global average pooling.

## References

- Avants, B. B.; Tustison, N.; Song, G.; et al. 2009. Advanced normalization tools (ANTs). *Insight j*, 2: 1–35.
- Balakrishnan, G.; Zhao, A.; Sabuncu, M. R.; Guttag, J.; and Dalca, A. V. 2018. An unsupervised learning model for deformable medical image registration. In *Proceedings of the IEEE Conference on Computer Vision and Pattern Recognition*, 9252–9260.
- Balakrishnan, G.; Zhao, A.; Sabuncu, M. R.; Guttag, J.; and Dalca, A. V. 2019. Voxelmorph: a learning framework for deformable medical image registration. *IEEE Transactions on Medical Imaging*, 38: 1788–1800.
- Cai, N.; Chen, H.; Li, Y.; Peng, Y.; and Li, J. 2020. Adaptive weighting landmark-based group-wise registration on lung DCE-MRI images. *IEEE Transactions on Medical Imaging*, 40: 673–687.
- Chen, J.; Frey, E. C.; He, Y.; Segars, W. P.; Li, Y.; and Du, Y. 2022. Transmorph: Transformer for unsupervised medical image registration. *Medical Image Analysis*, 82: 102615.
- Cheng, X.; Zhang, T.; Lu, W.; Meng, Q.; Frangi, A. F.; and Duan, J. 2025. SACB-Net: Spatial-awareness Convolutions for Medical Image Registration. In *Proceedings of the Computer Vision and Pattern Recognition Conference*, 5227–5237.
- De Vos, B. D.; Berendsen, F. F.; Viergever, M. A.; Sokooti, H.; Staring, M.; and Išgum, I. 2019. A deep learning framework for unsupervised affine and deformable image registration. *Medical Image Analysis*, 52: 128–143.
- Dice, L. R. 1945. Measures of the amount of ecologic association between species. *Ecology*, 26: 297–302.
- Fischer, B.; and Modersitzki, J. 2008. Ill-posed medicine—an introduction to image registration. *Inverse Problems*, 24: 034008.
- Fischl, B. 2012. FreeSurfer. *Neuroimage*, 62: 774–781.
- Hu, B.; Zhou, S.; Xiong, Z.; and Wu, F. 2022. Recursive decomposition network for deformable image registration. *IEEE Journal of Biomedical and Health Informatics*, 26: 5130–5141.
- Hu, J.; Shen, L.; and Sun, G. 2018. Squeeze-and-Excitation Networks. In *Proceedings of IEEE/CVF Conference on Computer Vision and Pattern Recognition*, 7132–7141.
- Huttenlocher, D. P.; Klanderman, G. A.; and Rucklidge, W. J. 1993. Comparing images using the Hausdorff distance. *IEEE Transactions on Pattern Analysis and Machine Intelligence*, 15: 850–863.
- Jaderberg, M.; Simonyan, K.; Zisserman, A.; et al. 2015. Spatial transformer networks. *Advances in Neural Information Processing Systems*, 28.
- Jia, X.; Bartlett, J.; Chen, W.; Song, S.; Zhang, T.; Cheng, X.; Lu, W.; Qiu, Z.; and Duan, J. 2023. Fourier-net: Fast image registration with band-limited deformation. In *Proceedings of the AAAI Conference on Artificial Intelligence*, 1015–1023.
- Jia, X.; Bartlett, J.; Zhang, T.; Lu, W.; Qiu, Z.; and Duan, J. 2022. U-net vs transformer: Is U-net outdated in medical image registration? In *International Workshop on Machine Learning in Medical Imaging*, 151–160.
- Kang, M.; Hu, X.; Huang, W.; Scott, M. R.; and Reyes, M. 2022. Dual-stream pyramid registration network. *Medical Image Analysis*, 78: 102379.
- Kingma, D. P. 2014. Adam: A method for stochastic optimization. *arXiv preprint arXiv:1412.6980*.
- Klein, A.; and Tourville, J. 2012. 101 labeled brain images and a consistent human cortical labeling protocol. *Frontiers in neuroscience*, 6: 171.
- Liu, Y.; Zuo, L.; Han, S.; Xue, Y.; Prince, J. L.; and Carass, A. 2022. Coordinate translator for learning deformable medical image registration. In *International Workshop on Multiscale Multimodal Medical Imaging*, 98–109.
- Lv, J.; Wang, Z.; Shi, H.; Zhang, H.; Wang, S.; Wang, Y.; and Li, Q. 2022. Joint progressive and coarse-to-fine registration of brain MRI via deformation field integration and non-rigid feature fusion. *IEEE Transactions on Medical Imaging*, 41: 2788–2802.
- Ma, J.; Zhang, Y.; Gu, S.; An, X.; Wang, Z.; Ge, C.; Wang, C.; Zhang, F.; Wang, Y.; and Yanan Xu, e. a. 2022. Fast and Low-GPU-memory abdomen CT organ segmentation: The FLARE challenge. *Medical Image Analysis*, 82: 102616.
- Ma, T.; Zhang, S.; Li, J.; and Wen, Y. 2024. IIRP-Net: iterative inference residual pyramid network for enhanced image registration. In *Proceedings of the IEEE/CVF Conference on Computer Vision and Pattern Recognition*, 11546–11555.
- Meng, M.; Feng, D.; Bi, L.; and Kim, J. 2024. Correlation-aware coarse-to-fine mlps for deformable medical image registration. In *Proceedings of the IEEE/CVF Conference on Computer Vision and Pattern Recognition*, 9645–9654.
- Mok, T. C.; and Chung, A. C. 2020. Large deformation diffeomorphic image registration with laplacian pyramid networks. In *Proceedings of Medical Image Computing and Computer Assisted Intervention*.
- Rana, S.; Hampson, R.; and Dobie, G. 2019. Breast cancer: model reconstruction and image registration from segmented deformed image using visual and force based analysis. *IEEE Transactions on Medical Imaging*, 39: 1295–1305.
- Shattuck, D. W.; Mirza, M.; Adisetiyo, V.; Hojatkashani, C.; Salamon, G.; Narr, K. L.; Poldrack, R. A.; Bilder, R. M.; and Toga, A. W. 2008. Construction of a 3D probabilistic atlas of human cortical structures. *Neuroimage*, 39: 1064–1080.

Taha, A. A.; and Hanbury, A. 2015. Metrics for evaluating 3D medical image segmentation: analysis, selection, and tool. *BMC Medical Imaging*, 15: 1–28.

Wang, H.; Ni, D.; and Wang, Y. 2024. Recursive deformable pyramid network for unsupervised medical image registration. *IEEE Transactions on Medical Imaging*, 43: 2229–2240.

Wang, H.; and Wang, Y. 2025. Equivariance and motion-enhanced Neighborhood Attention-based Pyramid network for 3D deformable medical image registration. *Biomedical Signal Processing and Control*, 108: 107897.

Zhao, S.; Dong, Y.; Chang, E. I.; Xu, Y.; et al. 2019a. Recursive cascaded networks for unsupervised medical image registration. In *Proceedings of the IEEE/CVF International Conference on Computer Vision*, 10600–10610.

Zhao, S.; Lau, T.; Luo, J.; Chang, E. I.-C.; and Xu, Y. 2019b. Unsupervised 3D end-to-end medical image registration with volume tweening network. *IEEE Journal of Biomedical and Health Informatics*, 24: 1394–1404.

Zhou, S.; Hu, B.; Xiong, Z.; and Wu, F. 2023. Self-distilled hierarchical network for unsupervised deformable image registration. *IEEE Transactions on Medical Imaging*, 42: 2162–2175.

## A Datasets and Implementation Details

**Datasets:** To comprehensively assess the performance of the proposed TCIP, we compare it against different registration models on three public MRI datasets, namely LPBA (Shattuck et al. 2008), Mindboggle (Klein and Tourville 2012), IXI (Avants et al. 2009), and one abdomen CT dataset FLARE (Ma et al. 2022). We preprocess these four datasets as follows. The LPBA dataset contains 40 T1-weighted MRI volumes, each annotated with 54 manually labeled Regions of Interest (ROIs). All volumes have been rigorously pre-aligned to the MNI 305. Specifically, each volume is cropped to  $160 \times 192 \times 160$  voxels with an isotropic voxel size of 1 mm. We use 31 volumes for training and 9 for testing, following the prior study (Wang, Ni, and Wang 2024). For the Mindboggle dataset, we choose the NKI-RS-22 and NKI-TRT-20 sub-datasets from Mindboggle101 as the training set and OASIS-TRT-20 as the test set, following the prior study (Ma et al. 2024). We crop each volume to  $160 \times 192 \times 160$  with an isotropic voxel size of 1 mm, while all images are pre-aligned with the MNI 152 template space. The IXI dataset contains the original brain MRI images provided by (Fischl 2012) and their corresponding 3D volume data after affine registration. All volumes are resampled to a voxel size of  $80 \times 96 \times 112$  (isotropic voxel size of 2 mm), and for training, we use 407 3D volumes (total  $407 \times 406$  paired samples), and for testing, 58 volumes (total  $58 \times 57$  paired samples), following the prior study (Wang, Ni, and Wang 2024). The FLARE dataset consists of 361 scans annotated with four organ labels, namely liver, kidney, spleen, and pancreas. Each volume is cropped to  $160 \times 192 \times 160$  voxels with an isotropic voxel size of 2.5 mm. We allocate 341 volumes for training and 20 for testing following the (Ma et al. 2024).

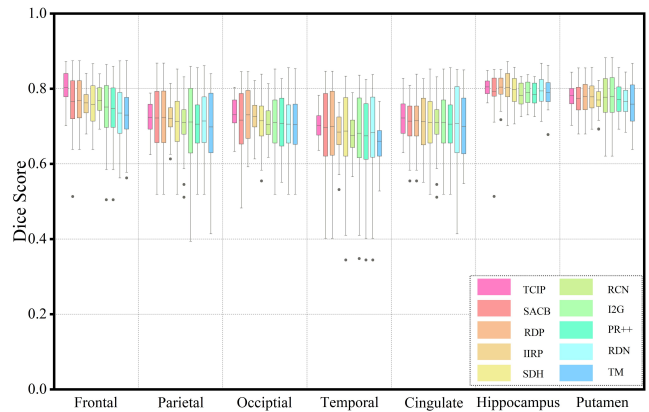


Figure C.1: Performance comparison of different models in seven regions of the LPBA dataset.

**Metrics:** To comprehensively assess the performance of various registration models, we adopt multiple quantitative metrics. The Dice score (Dice 1945) measures region-wise overlap, while the 95% maximum Hausdorff Distance (HD95) (Huttenlocher, Klanderman, and Rucklidge 1993) and the Average Symmetric Surface Distance (ASSD) (Taha and Hanbury 2015) quantify the similarity of the regional profiles. The quality of the estimated deformation field  $\phi$  is assessed by the percentage of voxels with non-positive Jacobian determinant  $|J_\phi|_{<0} \downarrow$  (i.e., folded voxels). In addition, we report Mean Squared Error (MSE), Inference Time (s), and model size (the number of parameters) for a comprehensive performance analysis.

**Implementation Details:** Our Model is implemented using Pytorch and trained on an NVIDIA GeForce RTX 4090 GPU. Following the prior study (Ma et al. 2024), we normalize all images to the range  $[0, 1]$ , optimize using the ADAM optimizer (Kingma 2014) at a learning rate of  $1 \times 10^{-4}$ , and set the size of volumetric patch  $n$ , hyperparameter  $\lambda$ , and batch size to 9, 1, and 1, respectively. In FERM, we adopt a reduction ratio  $r = 16$ . In TCI, we set the window size  $t$  and the maximum number of iterations  $k_{max}$  to 3 and 10, respectively.

## B Performance Comparison on HD95, ASSD, and MSE Metrics

In Table B, we present the performance of different registration models on the Mindboggle, LPBA, and IXI datasets, evaluated by the HD95, ASSD, and MSE metrics. The experimental results demonstrate that TCIP outperforms the other registration models in most scenarios and achieves SOTA results on at least two metrics for each dataset.

## C Quantitative Analysis on Different Anatomical Structures

Following the prior study (Wang, Ni, and Wang 2024), we evaluate TCIP’s registration performance on selected regions in both hemispheres to assess its accuracy across diverse anatomical structures. Specifically, Figure C.1

Table B: Performance comparison of different registration models on the Mindboggle, LPBA, and IXI datasets evaluated by HD95, ASSD, and MSE metrics

	Model	Mindboggle			LPBA			IXI		
		HD95↓	ASSD↓	MSE (10 <sup>-3</sup> )	HD95↓	ASSD↓	MSE (10 <sup>-3</sup> )	HD95↓	ASSD↓	MSE (10 <sup>-3</sup> )
U-Net	VM (CVPR'18)	5.683	1.726	7.449	6.557	2.089	2.293	1.460	0.584	0.727
	TM (MIA'22)	5.399	1.561	5.500	6.439	1.962	1.179	1.432	0.557	0.432
Cascade	RCN (ICCV'19)	5.090	1.439	4.607	5.817	1.777	2.005	1.397	0.563	0.518
	SDH-Net (TMI'23)	5.047	1.413	4.616	5.750	1.682	0.963	1.362	0.510	0.392
Pyramid	RDN (JBHI'22)	5.041	1.468	5.884	5.817	1.747	1.365	1.270	0.512	0.570
	PR++ (MIA'22)	5.312	1.510	4.871	6.060	1.778	0.852	1.290	0.508	0.360
	I2G (MMMI'22)	5.129	1.474	4.347	5.646	1.665	1.018	1.301	0.509	0.408
	RDP (TMI'24)	4.992	1.392	4.191	5.618	1.621	0.633	1.229	0.472	0.234
	IIRP (CVPR'24)	4.947	1.393	4.163	5.737	1.605	0.623	<b>1.225</b>	0.476	0.236
	SACB (CVPR'25)	<b>4.884</b>	1.386	4.852	5.862	<b>1.326</b>	0.837	1.297	0.504	0.351
	<b>TCIP (ours)</b>	4.909	<b>1.375</b>	<b>3.969</b>	<b>5.577</b>	1.657	<b>0.614</b>	1.229	<b>0.470</b>	<b>0.230</b>

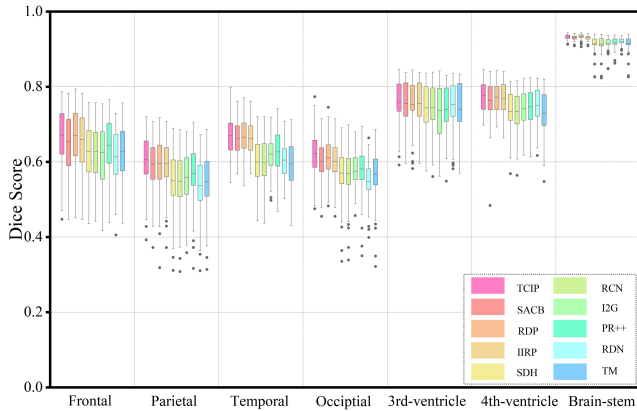


Figure C.2: Performance comparison of different models in seven regions of the Mindboggle dataset.

presents the Dice scores for seven brain regions in the LPBA dataset, including the frontal, parietal, temporal, occipital, cingulate, hippocampus, and putamen. Figure C.2 presents the Dice scores for 7 brain regions in the Mindboggle dataset, including the frontal, parietal, temporal, occipital, third ventricle, fourth ventricle, and brainstem. Figure C.3 presents the Dice score across 30 regions of the IXI dataset. All these experimental results demonstrate that TCIP outperforms existing registration models.

## D Effectiveness of TCI at Each Decoding Layer

In this section, we conduct ablation studies to assess the effectiveness of TCI at each decoding layers. Omitting TCI at a given layer fixes the number of iterations to one, thereby preventing iterative refinement of the deformation field. As shown in Table D, progressively enabling TCI across additional layers steadily improves TCIP's performance. No-

Table D: Ablation study on the effectiveness of TCI on various decoding layers

Layer 4	Layer 3	Layer 2	Layer 1	Mindboggle	LPBA	IXI
				64.1	71.5	79.8
✓				65.6	72.9	79.8
	✓			65.6	72.9	79.9
		✓		65.7	73.0	79.9
			✓	65.9	73.0	80.1
✓	✓			66.1	73.2	80.2
✓	✓	✓		66.3	73.3	80.4
✓	✓	✓	✓	<b>66.4</b>	<b>73.3</b>	<b>80.5</b>

Table E: Ablation study on thresholds  $\delta_s$  and  $\delta_c$  values

		Mindboggle		LPBA		IXI	
$\delta_s$	$\delta_c$	0.01	0.005	0.01	0.005	0.01	0.005
0.01		65.9	66.1	73.1	73.2	80.4	80.4
	0.005	66.2	<b>66.4</b>	73.2	<b>73.3</b>	80.5	<b>80.5</b>
	0.001	66.2	66.2	73.1	73.1	80.4	80.2

tably, applying TCI at higher-resolution layers (e.g., Layer 1) yields larger performance gains than at lower-resolution layers (e.g., Layer 4). A plausible reason for this is that higher-resolution feature maps more closely match the original image dimensions, preserving fine-grained structural details. Consequently, determining the number of iterations for higher-resolution layers yields greater performance improvements.

## E Impact of Varying Values of Thresholds

In this section, we investigate the sensitivity of the predetermined thresholds  $\delta_s$  and  $\delta_c$ . As shown in Table E, these two thresholds exhibit low sensitivity to variation and have minimal impact on the overall performance of TCIP. Nonethe-

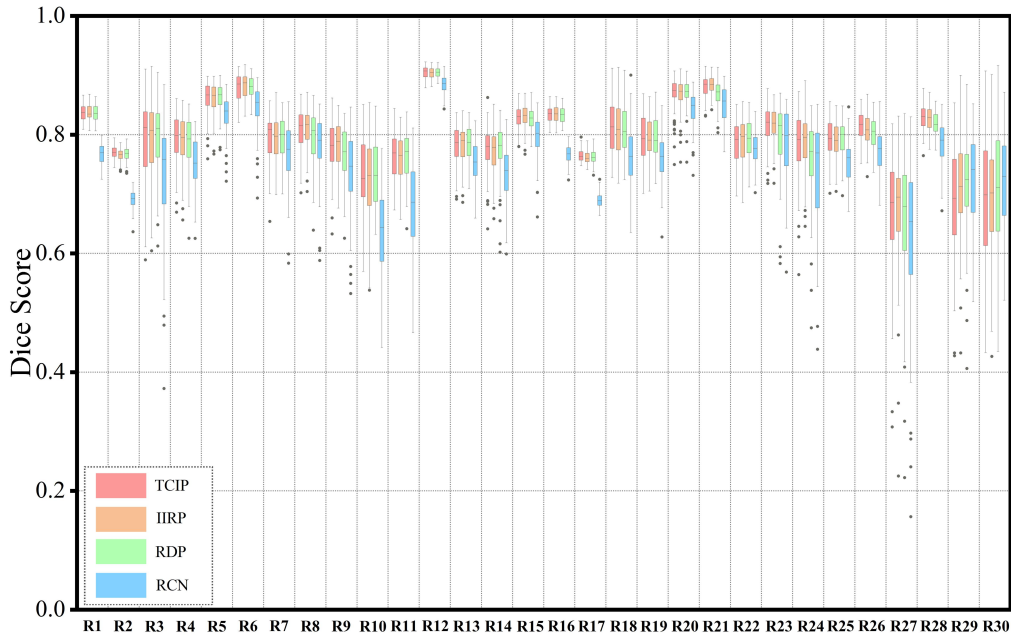


Figure C.3: Performance comparison of different models in thirty regions of the IXI dataset.

Number of iterations	Layer			
	Layer 4	Layer 3	Layer 2	Layer 1
10	0.00	0.00	0.00	0.00
9	0.00	0.00	0.00	0.00
8	0.00	0.00	0.00	0.00
7	0.00	0.00	0.00	0.00
6	0.00	0.00	0.00	0.00
5	0.00	0.00	0.00	0.00
4	99.37	48.85	26.28	0.00
3	0.63	51.15	73.72	100.00
2	0.00	0.00	0.00	0.00
1	0.00	0.00	0.00	0.00

Figure E: Statistics of the number of iterations across different decoding layers.

less, we choose the middle range values, i.e.,  $\delta_s = 0.005$  and  $\delta_c = 0.005$ , which yield the best performance

In addition, in Figure E, we present the number of iterations per decoding layer determined by TCI on the IXI dataset. The experimental results demonstrate that three or four iterations suffice for convergence in most cases. Hence, our predefined maximum number of iterations  $K_{max} = 10$

Table F: Ablation study on the effectiveness of different similarity metrics adopted in TCI

		MAE		MSE		NCC		
		0.01	0.005	0.01	0.005	0.01	0.005	
$\delta_s$	$\delta_c$	0.01	79.6	79.7	80.0	79.5	80.4	80.5
	0.005	79.7	80.0	79.9	80.1	80.5	<b>80.5</b>	
	0.001	80.2	79.1	80.1	79.9	80.4	80.2	

is reasonable.

## F Impact of Different TCI Similarity Metrics

In this section, we examine the effect of three similarity metrics, namely Normalized Cross-Correlation (NCC), Mean Absolute Error (MAE), and Mean Squared Error (MSE), on the performance of TCI. As shown in Table F, NCC delivers the best results. Hence, we adopt NCC as the similarity metric for all experiments in this paper.

## G Impact of Different Sliding Window Sizes

In Table G, we present the effect of window size  $t$  on the performance of TCIP. On the IXI dataset, increasing  $t$  from 3 to 4 yields marginal performance gains but incurs longer inference time. Increasing  $t$  further to 5 degrades performance across all metrics, suggesting that  $t = 4$  provides sufficient iterative refinement without incurring excessive iterations. On the Mindboggle dataset, setting  $t = 3$  outperforms  $t = 4$  on most metrics, likely because  $t = 4$  induces excessive iterations in TCI's deformation refinement. Therefore, we set  $t = 3$  for all experiments in this paper.

Table G: Ablation study on the different window sizes

<b>IXI</b>					
<i>t</i>	Dice	HD95	ASSD	MSE	time
3	80.4	1.23	0.48	0.24	<b>0.09</b>
4	<b>80.9</b>	<b>1.22</b>	<b>0.46</b>	<b>0.21</b>	0.15
5	80.7	1.27	0.49	0.23	0.29
<b>Mindboggle</b>					
<i>t</i>	Dice	HD95	ASSD	MSE	time
3	<b>66.4</b>	<b>4.91</b>	1.38	3.97	<b>0.16</b>
4	66.1	4.93	1.38	<b>3.89</b>	0.22
5	65.8	4.94	1.39	4.06	0.35